Appl Phys B (2011) 104:409–425
DOI 10.1007/s00340-011-4373-y

Applied Physics B
Lasers and Optics

Sooting turbulent jet flame: characterization and quantitative soot measurements

M. Köhler · K.P. Geigle · W. Meier · B.M. Crosland · K.A. Thomson · G.J. Smallwood

Received: 18 October 2010 / Revised version: 7 December 2010 / Published online: 5 February 2011

Abstract Computational fluid dynamics (CFD) modelers require high-quality experimental data sets for validation of their numerical tools. Preferred features for numerical simulations of a sooting, turbulent test case flame are simplicity (no pilot flame), well-defined boundary conditions, and sufficient soot production. This paper proposes a non-premixed C_2H_4/air turbulent jet flame to fill this role and presents an extensive database for soot model validation.

The sooting turbulent jet flame has a total visible flame length of approximately 400 mm and a fuel-jet Reynolds number of 10,000. The flame has a measured lift-off height of 26 mm which acts as a sensitive marker for CFD model validation, while this novel compiled experimental database of soot properties, temperature and velocity maps are useful for the validation of kinetic soot models and numerical flame simulations. Due to the relatively simple burner design which produces a flame with sufficient soot concentration while meeting modelers' needs with respect to boundary conditions and flame specifications as well as the present lack of a sooting "standard flame", this flame is suggested as a new reference turbulent sooting flame.

The flame characterization presented here involved a variety of optical diagnostics including quantitative 2D laser-induced incandescence (2D-LII), shifted-vibrational coherent anti-Stokes Raman spectroscopy (SV-CARS), and particle image velocimetry (PIV). Producing an accurate and comprehensive characterization of a transient sooting flame was challenging and required optimization of these diagnostics. In this respect, we present the first simultaneous, instantaneous PIV, and LII measurements in a heavily sooting flame environment. Simultaneous soot and flow field measurements can provide new insights into the interaction between a turbulent vortex and flame chemistry, especially since soot structures in turbulent flames are known to be small and often treated in a statistical manner.

Keywords Soot · Jet flame · Laser diagnostics · Turbulent combustion · Laser-induced incandescence · Validation data

M. Köhler (✉)
Institut für Verbrennungstechnik, Deutsches Zentrum für Luft- und Raumfahrt (DLR), Pfaffenwaldring 38-40, 70569 Stuttgart, Germany
e-mail: M.Koehler@dlr.de
Fax: +49-711-6862-578

M. Köhler · K.P. Geigle · W. Meier
German Aerospace Center, Institute of Combustion Technology, Stuttgart, Germany

B.M. Crosland
Department of Mechanical & Aerospace Engineering, Carleton University, Ottawa, Canada

K.A. Thomson · G.J. Smallwood
Institute for Chemical Process and Environmental Technology, National Research Council, Ottawa, Canada

1 Introduction

The emission of particulate matter from aircraft gas turbine engines, their potential impact on world climate and human health, and state-of-the-art methods for measuring particulate matter in aircraft engine exhaust are key issues concerning international bodies such as the ICAO, EASA, and FAA [1, 2]. Significant progress has been made in non-volatile particulate matter diagnostics in aircraft engines, presented in the Aerospace Information Report (AIR) 5892 [3] and the respective Technical Annexes (TA) as AIR 6037 [4]. These Aerospace Recommended Practice (ARP) style documents include detailed descriptions of techniques and methods applicable for measurements of particle mass (TA-1), particle

number, and particle size (TA-2). However, for the development of new ARP guidelines to replace the current SAE smoke number measurements in aero-engine certification processes, extensive research on alternative soot measurement methods is needed.

Additionally, new combustion chamber geometries and injector concepts may be needed to fulfill increasingly stringent emission rules, making deeper understanding of the soot formation process more important than ever [5]. Besides its negative environmental and health effects, soot production within gas turbine combustion chambers is unwanted as it decreases the combustion efficiency and enhances thermal radiation, making soot a limiting factor in operability. Therefore, economic as well as environmental motivations are directly linked to the understanding of soot formation.

To improve soot predictions for gas turbine engines and industrial combustors, numerical simulations and kinetic soot model schemes need to be developed and adopted to relevant conditions that can accurately treat turbulent mixing, combustion and particularly the complex chemistry of soot formation. One of the most demanding problems in this respect is the complexity of the formation process, which is still under investigation even today [6–9]. Current numerical developments are divided in two directions according to individual requirements in application. One approach emphasizes accurate, but computationally-expensive models, making the application to a technical configuration unfeasible [6, 10, 11]. The other approach is to focus on simplified models that are less accurate but allow application to more complex burner configurations [12, 13]. A recent approach by Di Domenico proposes to bridge the gap between these two approaches with a soot model that seems to allow an accurate, yet affordable calculation of soot in complex gas turbine combustion chambers [14]. However, to evaluate the quality of different available numerical approaches experimental data for validation purposes focusing on technically relevant combustion processes is strongly needed.

Bound to this indispensable experimental data, certain conditions and features are desired from a modelers' perspective. In this paper, our goal is to provide a database for model validation purposes in close collaboration with modelers in order to match these desires as close as possible to experimental feasibility. Hence, we are trying to fill the gap in recent turbulent combustion history, where appropriate experimental databases have not fully met current modelers' needs with respect to burner design, boundary conditions, and soot concentrations [14, 15].

Favored, both from numerical as well as an experimental viewpoint, is a simple, well-defined burner geometry without the need for a pilot flame. This is especially true with respect to easy reproducibility. Bluff body, spray, and swirl flames have proven to be more challenging for inter-laboratory comparisons as compared to burners with simpler flow passages and simpler construction properties. Therefore, a long undisturbed fuel line producing fully-developed flow at the exit is desired. All these aspects are inherent to simple jet burners thus making them the obvious first choice.

Of equal priority for validation experiments is the consideration of the boundary conditions [16]. Great care must be taken in setting and measuring the boundary conditions to allow proper definition of the computational problem [17, 18]. In an ideal situation, the boundary conditions of the experiment are consistent with the available input features of the models. As pointed out by Barlow, modelers should be consulted during the burner design phase; flame behavior can be very sensitive to small variations in boundary conditions, even for burners with simple geometries and, especially with regard to their appropriate measurement [16, 19].

Another major aspect of validation flame selection is the choice of flame conditions such as turbulence intensity on the one side and fuel on the other side. A balance must be struck between soot concentration, reasonable turbulence, and simplicity. Reynolds numbers above 7500 with considerable soot production are favored, but simple fuels are desired for current chemistry model validation, leaving increased fuel complexity for future iterations. Generally, addition of other fuels to the main fuel proves no problem from either an experimental or modeling perspective, but reaction mechanisms get larger and validation becomes more challenging [15].

Directly linked to the choice of flow parameters are the dimensions of the system. The flame itself should be short enough to have well-defined air flow boundary conditions even high up in the flame. This is also strongly favored from a diagnostic point of view because a short flame reduces the number of measurement locations and results in a less complex flame in terms of enclosure, optical accessibility, and air handling in the laboratory.

Taking all the desires into account, setting up an appropriate database for validation, and especially turbulent soot model validation, becomes an ambitious task and useful past experience can be drawn from the literature. These challenges in validation of turbulent combustion models are not a new topic by any means. For example, experimental data on simple non-sooting turbulent reacting flows was documented in review papers [20–22] and [23] more than 20 years ago, but were found to be inappropriate for validation purposes at that time. The accountability committee of leading combustion researchers concluded that none of the available data sets were appropriate for model validation and the computational effort should not be initiated at that time. This conclusion highlights the fact that experiments not specifically designed for the purpose of model validation are unlikely to be useful for that purpose [19]. Targeted

research in the following years (in particular from the Turbulent Non-Premixed Flame workshop) resulted in much better exchange and collaborations to build the vast and rich understanding we have of turbulent combustion models today [24].

Measurements of sooting, turbulent non-premixed flames suitable for validation purposes, however, have been excluded from this satisfying development. This is reflected by the scarcity of available data sets. Lee at al. conclude that the reason for this development is associated with the difficulty of making comprehensive in-situ measurements in an environment dominated by large fluctuations in the velocity field and various parameters of interest (temperature, species concentrations) [25]. Although these measurements would be of great interest to science and practical applications for the reduction of pollutant formation, experimental data sets based on modelers' needs are surprisingly rare in literature.

First measurements of soot in a turbulent diffusion flame are reported from Kent and Bastin in 1984 [26] and have led to a description of the soot field in flames. Early systematic soot investigations in turbulent ethylene flames were reported by Kent and Honnery [27] in 1987. A mean soot volume fraction of 1.8 ppm was measured and correlations between soot concentrations and mean mixture fractions at several height locations in a series of flames allowed substantial basic understanding of soot formation processes. One significant result is that the total mass flow of soot at a given height in the growth region is a continuous function of time, independent of the flame size. Nowadays, however, greater accuracy in the experimental setup and data collection is demanded by modelers. Those early experiments suffer most of all from poorly defined boundary conditions, making them unsuitable for current model validation purposes. In addition to these higher demands, diagnostics themselves have evolved in recent years, allowing for better precision and accuracy.

The very same arguments apply to the jet flame measurements of Coppalle and Joyeux [28], which can be compared to those of Kent and Honnery. Coppalle and Joyeux verified those measurements with intrusive techniques, obtaining results that are quite similar, but which expand on time-resolved particle concentrations. While introducing new experimental methods, the validation data set itself is not significantly enhanced or improved due to limitations in the diagnostic tools at hand.

Although not state-of-the-art any more and far from an ideal dataset discussed above, the presented experimental data from Kent and Honnery, as well as from Coppalle and Joyeux is still of great interest and used for validation purposes in recent years [29]. The need for updated data is exemplified by Lindstedt and Louloudi's use of this 18-year old data to validate their joint-scalar transported PDF model. On the other hand, this shows that the quality of the old data could not be reproduced or improved since then.

Vander Wal [30] presented data in 1997 for measurements made in a lifted turbulent jet-flame using advanced optical diagnostic techniques. These simultaneous LII and LIF measurements were published only for selected parts of the flame and provide no quantitative data on soot or polycyclic aromatic hydrocarbons (PAH). An exhaustive search of the current literature indicates that data providing a well-defined co-flow and crucial information on temperature and velocity fields are not available for this flame and, therefore, the described data set does not meet current modelers' requirements.

In 1999, Brookes and Moss presented sampling measurements for a piloted methane flame with well-defined boundary conditions. They inferred the mixture fraction from measurements of the air-to-fuel ratio that were made using a mass spectrometer on the extracted sample. The temperature field was measured using a thermocouple and quantitative optical soot measurements by laser extinction tomography [31]. The data was used to validate a numerical study a year later by Kronenburg et al. [32]. Unfortunately, due to the small average soot concentration of 0.16 ppm, the large 600 mm length of the flame, the relatively low turbulence (Reynolds number of 5000), and the modeling complexity introduced by the pilot flame, this data is not fully satisfactory for recent needs in turbulent soot modeling.

Extensive work on statistical analyses of time-averaged and instantaneous soot volume fractions from simple jet, precessing jet and bluff body burners were conducted by Qamar et al. [33]. While new details of the effect of global mixing rates on soot in turbulent flames were revealed, the flames are difficult to reproduce in many labs due to its lengths from 700 to 1100 mm. Perhaps more importantly, data on temperature and velocity fields, crucial for model validation, are absent. Xin and Gore [34] presenting significantly higher soot concentrations with averages of 0.8 ppm for a 7.1 cm pipe diameter non-premixed turbulent buoyant ethylene flame, but do not include any data beyond the soot characteristics.

Recently, several groups have performed comprehensive studies of turbulent non-premixed flames with an emphasis on providing high-quality experimental validation data [25, 35, 36]. However, these valuable systematic measurements have been conducted either in complex piloted burner flames (providing additional challenges to modelers), large scale flames (obscuring the boundary conditions in the upper portion of the flame), or provide very low soot concentrations (making use in general soot model validation difficult) [15].

In the present work, we contribute a data set designed for validation of a turbulent non-premixed sooting jet flame with special emphasis on CFD modelers' needs by a) definition of a simple turbulent sooting flame with specified

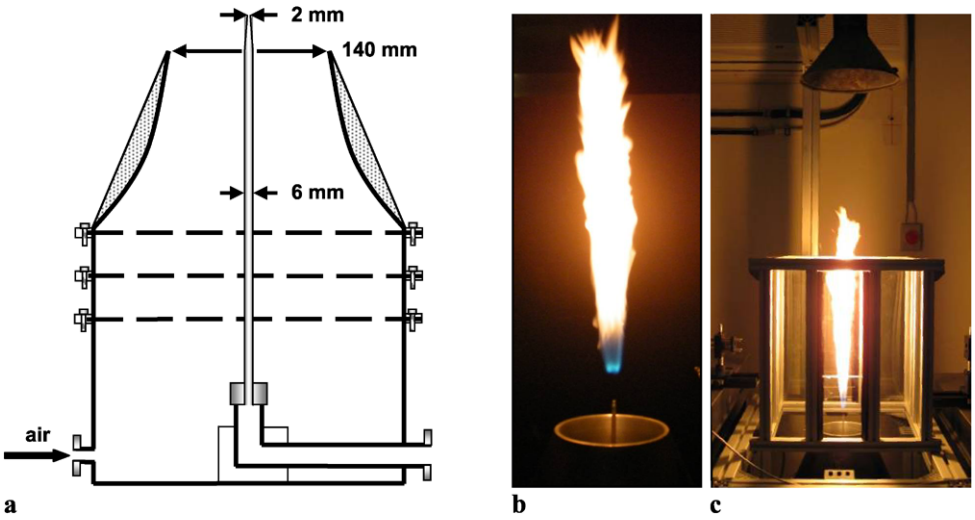

Fig. 1 **a** Burner schematic, **b** photograph of lifted jet flame, **c** jet burner in optical housing for defined boundary conditions

boundary conditions and b) the acquisition of high-quality experimental data sets. Extensive information on crucial flame parameters for model validation are provided including detailed temperature information, velocity field data and quantified soot concentrations. Simultaneous to the LII measurements, OH* chemiluminescence is detected and used to evaluate the time-averaged axi-symmetry of the flame.

2 Experimental

2.1 Burner configuration

Taking all the above discussion on the requirements and conditions into account, we found the best match to be an atmospheric non-premixed ethylene jet flame. Ethylene has proven to be a reasonable soot source in turbulent combustion [33, 34, 37]. From a chemical point of view, ethylene is formed early in the combustion of many larger hydrocarbons as an intermediate species [38] and so should be a component of existing kinetic models.

The burner schematic and flame photographs are shown in Fig. 1. The burner consists of a circular nozzle of 2.0 mm inner diameter from which the fuel emerges. The tube has an external diameter of 6 mm and tapers to a sharp edge at the jet-exit. Co-annular dry air flows through a contoured nozzle which converges from an inner diameter of 280 mm to 140 mm over a vertical distance of 310 mm and provides a homogeneous co-flow of oxidizer. Figure 1(b) shows a picture of the sooting flame. To further shield the flame from air currents in the laboratory, the burner was mounted inside an optically accessible housing, shown in Fig. 1(c).

The flame conditions for the selected lifted turbulent flame are listed in Table 1. The visible flame height is 400–500 mm and the lift-off height defined here as the position where the OH* chemiluminescence reached its maximum value was 26 mm. Although there is no consistency in the literature regarding the definition of the lift-off height, the presented definition is well suited for a comparison with CFD simulations. In addition, the lift-off height was determined experimentally by passing a laser beam through the flame and adjusts its height relative to the burner tip until it overlaps the lowest visible flame. The experiments showed that the visible lift-off region determined by eye is in fact a few millimeters higher than the optically determined OH* lift-off height, but is ideally suited as simple and fast indicator for flame reproducibility. All experiments were conducted at atmospheric pressure with an exhaust hood placed 1.5 m above the nozzle; no influence of the exhaust hood on the flame could be detected.

Table 1 Operating conditions for the sooting, turbulent ethylene flame. Listed ranges cover different experimental days

Absolute ambient pressure	959–981 mbar
Exit Reynolds number	10 000
Fuel mass flow	10.4 g min^{-1}
Air mass flow	320 g min^{-1}
Fuel temperature	297 ± 5 K
Air temperature	311 ± 5 K
Mean fuel jet velocity	44 m s^{-1}
Power	8.7 kW
Lift-off height	26 mm

2.2 Soot measurements

2.2.1 Simultaneous LII and OH measurements*

Soot measurements were performed using planar LII and calibrated by extinction measurements recorded at a different time in the same flame. The optical configuration for the

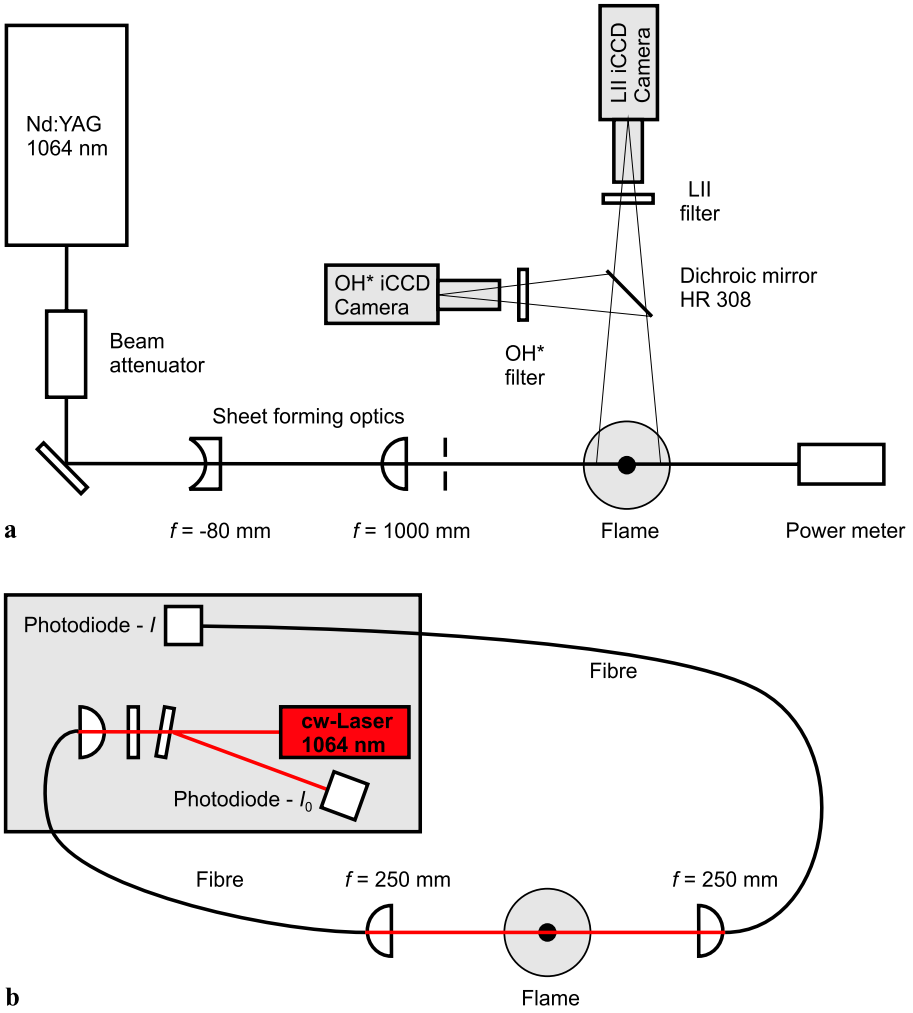

Fig. 2 **a** Experimental setup for simultaneous LII and OH* chemiluminescence measurements. **b** Optical setup for the extinction measurement to calibrate the LII signal. The line-integrated LII signal is correlated to the line-of-sight attenuation along the same line at $h = 300$ mm

simultaneous two-dimensional LII and OH* chemiluminescence measurements is shown in Fig. 2(a).

A 10 Hz pulsed Nd:YAG laser (Spectra Physics, GCR3-290) emitting at 1064 nm with a pulse duration of 7 ns was used for the LII excitation. Optics ($f = -80$ mm cylindrical lens, $f = 1000$ mm spherical lens) formed the beam into a sheet. A rectangular aperture was used to block the low fluence edges of the sheet, producing a sheet 40 mm tall and 0.2 mm thick. The laser sheet was imaged onto a beam profiler (WinCam-UCM, Dataray) using a spherical lens ($f = 500$ mm) and NG filters (Laser 2000) and is shown in Fig. 3(a). The complete characterization of the laser beam is displayed in Fig. 3(b)–(d), showing horizontal and vertical fluence profiles along with the fluence distribution of the laser sheet at the focus. To ensure the LII signal is as independent of the laser energy as possible, it is commonly suggested for soot mapping to remain in the LII 'plateau' region [39]. In this case, a total energy of 40 mJ, corresponding to a laser fluence of approximately 0.5 J/cm^2 was selected based on the fluence curve included in Fig. 3(e) (as recommended in [40] for turbulent flames). The laser sheet pulse energy was adjusted to 40 mJ using an attenuator composed of a half-wave plate and a Glan polarizer. The laser energy was monitored during the experiments with a Scientech 364 power meter.

The LII emission was detected normal to the laser sheet by an intensified interline frame transfer CCD camera (Dicam Pro, PCO, 1280 × 1024 pixels) capable of interframe times as short as 500 ns. A first gate of 60 ns duration before the laser shot was used to acquire the background flame luminosity and a second gate with the same duration started simultaneously with the laser pulse to acquire the LII signal. The camera was equipped with an interference filter (LOT 450 FS40-50) transmitting LII radiation centered at $\lambda = 450 \pm 10$ nm and a Nikon VIS lens ($f = 105$ mm, F2.5).

Simultaneous OH* chemiluminescence measurements were performed during the LII acquisitions. The OH* signal was separated from the LII by a dichroic mirror (Laser Components, HR 308 nm) and detected by an intensified CCD (iCCD) camera (Flamestar 2, LaVision, 384 × 286 pixels) equipped with an interference filter (Hugo Anders,

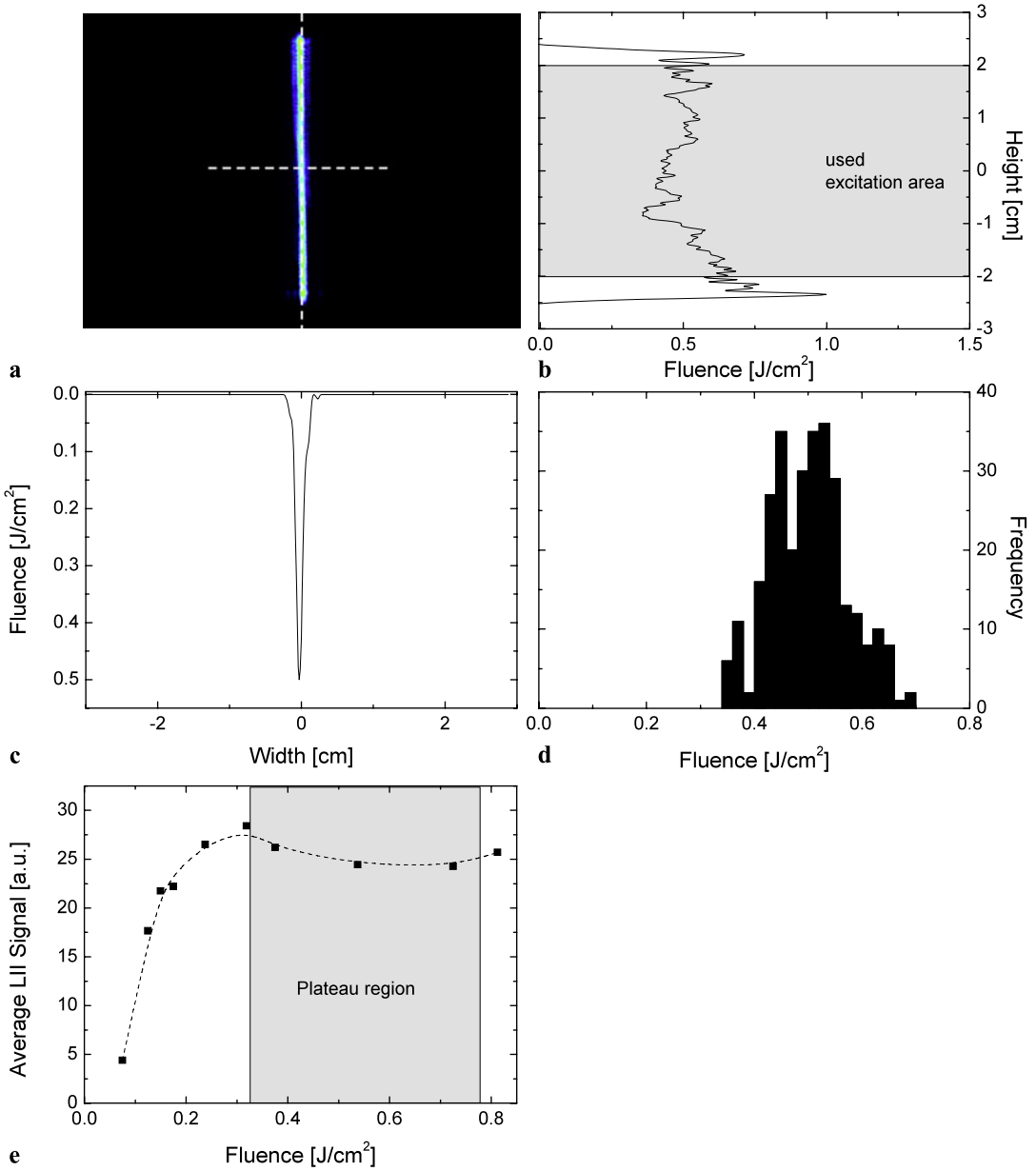

Fig. 3 Laser beam characteristics and resulting LII response curve for 1064 nm excitation. **a** Measured beam profile, **b** vertical profile along the axis, **c** horizontal profile and **d** energy distribution along the vertical axis. **e** LII response dependence on laser energy for given soot concentration. A cubic spline has been fit to the data to guide the eye

320 nm) and with a Halle UV lens ($f = 100$ mm, F2.0). The gate of this camera (150 µs duration) was delayed by 2 µs with respect to the laser pulse. Under the given experimental conditions (soot concentrations, flame dimension, and detection optics), preliminary tests showed that soot emission in the spectral OH* detection window is negligible. The frame rates of the cameras allowed the simultaneous LII and OH* chemiluminescence acquisition every 800 ms. Note, however, that direct comparisons of the LII and OH* chemiluminescence measurements are of limited value since LII measures the instantaneous soot concentrations in the laser excitation plane whereas OH* chemiluminescence provides line-of-sight integrated images for multiple planes. For tomographic reconstruction of the OH* chemiluminescence, an Abel inversion is performed on the line-of-sight integrated signal from both sides of the flame center line.

2.2.2 *Extinction measurements*

Figure 2(b) shows a schematic of the experimental setup for the extinction measurements used for LII calibration. A fiber-coupled laser system with a solid-state laser emit-

ting at a wavelength of 1064 nm (LCL-LCS-DTL-322-1000, Laser2000) was used for the extinction measurement. A prior study revealed [40] that near-infrared light is preferred for absorption measurements of soot particles because visible wavelengths are also absorbed by PAHs, a precursor species of soot. The laser light was coupled into a fiber (UV400, Avantes) and subsequently focused (f = 250 mm) into the flame. After passing through the flame at a height of $h = 300$ mm above the burner nozzle tip, the beam was collimated into a similar fiber directly mounted to a photodiode (PDA520, Thorlabs). Laser energy fluctuations were monitored by measuring the intensity of a back-reflection of the incident laser beam from a quartz plate by a second photodiode. Temperature drifts were found to cause variations in absorption of up to 8% during initial measurements. A custom-made thermal stabilization device was employed on both photodiodes and found to reduce temperature-based variation in the baseline absorption to below 0.1%. Signal-to-noise ratio was greatly improved by frequency modulation of the laser emission in combination with frequency selective filtering. A function generator (GFG 2004, Iso-Tech) modulated the original laser emission with a defined frequency of 620 Hz that was monitored by a dual lock-in amplifier (Model 5105, Signal Recovery), which filters residual frequencies and increases the signal-to-noise ratio. The resulting signal was an average value taken over 5000 output data points from the lock-in amplifiers with a read-out sampling rate of 100 kHz.

The extinction experiment resulted in line-of-sight averaged soot concentrations, correlated to the LII signal integrated over the same line-of-sight. The resulting calibration constant was then used to calibrate the LII images. The soot volume fractions, f_V, were determined with the Beer–Lambert–Bouguer's law

$$\frac{I}{I_0} = \exp\left(\frac{K_e \cdot f_v \cdot L}{\lambda}\right) \tag{1}$$

in which I/I_0 is the ratio of the transmitted to incident light intensity, λ is the wavelength of the light and L is the optical path length in flame. Based on earlier investigations [40], the calculations were carried out using the index of refraction, m of $1.60–0.59i$, resulting in a dimensionless extinction coefficient K_e of 5.01 [41] for both the extinction (1064 nm) and LII detection wavelength (450 nm), while acknowledging that there is uncertainty in the correct value of the index of refraction to use [42–47]. The correlated time-averaged LII images of the flame were corrected for self-absorption by an 'onion peeling' algorithm [48] that was implemented into our data analysis routines [49] for DaVis (LaVision). The uncertainty of the measurements of the soot volume fraction, primarily due to the uncertainty in the value of the refractive index, was estimated to be ±15%. This value is in good agreement with the recent detailed analysis by Crosland et al., presenting a 95% confidence interval of 15% for 442 nm [50]. Combining this with an uncertainty of ±10% for the LII measurement based on signal intensity variations due to shot-to-shot laser fluctuations and inhomogeneities of the sheet in all three dimensions including occasional beam steering or laser absorption, the total uncertainty for the soot volume fraction is estimated to be 20%, similar to [51].

2.3 Temperature measurements

To determine temperature statistics in the fuel rich burning and sooting regions of the flame on a single-shot basis, shifted-vibrational CARS on N_2 was employed which avoids the drawback of spectral interference from laser-generated emission of the C_2 present in sooting flames suffered by standard nitrogen CARS. The optical setup used for this study (shown in Fig. 4) avoids this by shifting the nitrogen CARS signal to 518 nm where no C_2 emission is present [52].

For these SV-CARS measurements, the 532 nm emission of a Nd:YAG laser (GCR230, Spectra Physics) operated at 10 Hz was used to pump a customized dye laser system (Precision Scan, SIRAH Laser- und Plasmatechnik GmbH), composed of one narrowband ($\lambda = 582$ nm) unit and one broadband ($\lambda = 685$ nm) unit. The narrowband dye laser at 582 nm is operated with pyrromethene, (0.16 g/l in ethanol, Sirah) and has a maximum output of 42 mJ per pulse. The broadband dye laser uses pyridin-1 (0.25 g/l in ethanol, Sirah) with 31 mJ maximum power output per pulse.

To match the divergence of both dye laser beams and reduce the laser fluence on the optical components, the laser beams were expanded by a factor of 2 using Galilean telescopes. The energy of each beam was independently controlled by attenuators composed of a half-wave plate and a polarizer. The pulse energies used depended on the N_2 density at the measurement location and were in the range of 4–13 mJ for the broadband beam and 9–27 mJ for the narrowband beam. After the attenuator, the narrowband beam was split in two and the three laser beams were then focused in a folded BOXCAR geometry by a spherical lens ($f = 350$ mm). After recollimation the CARS signal was separated from the laser beams by an aperture and two dichroic mirrors, and subsequently focused into a fiber (UV400, Avantes). The CARS signal was dispersed on a double-grating spectrograph (Model 1403, Spex) and recorded by an iCCD camera (Flamestar 2F, LaVision). From a measurement without a flame, the spatial resolution was found to be $L_{95\%} = 2.2$ mm with a diameter of the probe volume of approximately 300 µm.

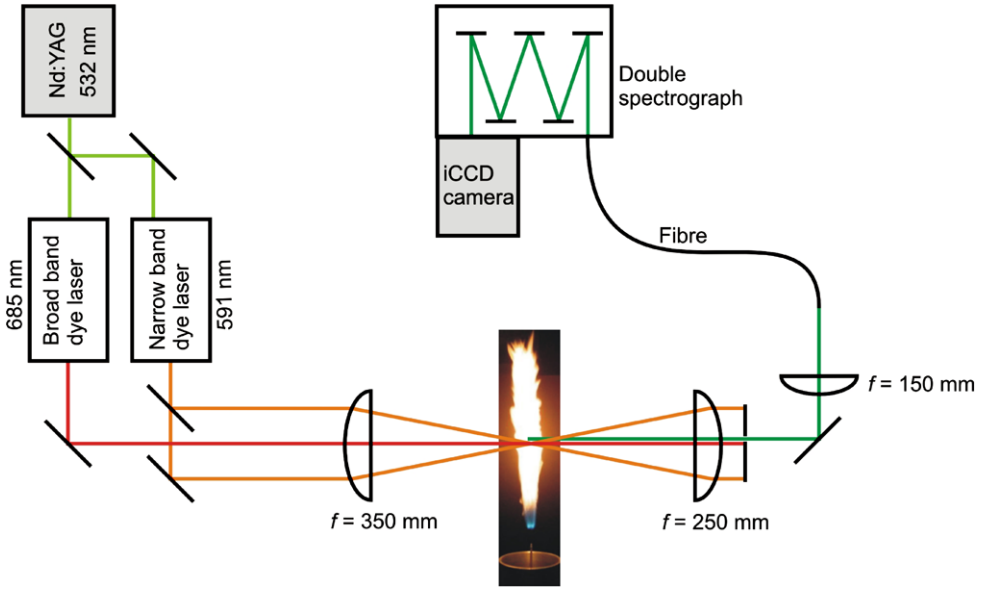

Fig. 4 Experimental setup for SV-CARS measurements

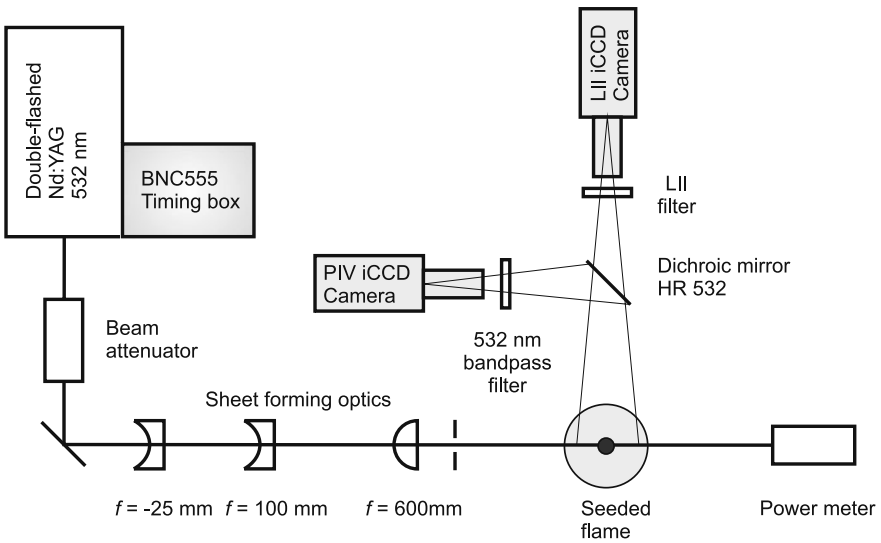

Fig. 5 Experimental setup for simultaneous PIV and LII measurements

2.4 Simultaneous PIV and LII measurements

Figure 5 shows the experimental setup for simultaneous PIV and 2D-LII measurements. A single cavity frequency-doubled Nd:YAG laser (Spitfire 600, InnoLas) frequency-doubled to 532 nm was operated such that the flash lamps were double-flashed and each flash was q-switched, producing a pair of laser pulses with an interpulse delay of 40 µs. The beam was passed through a combination of spherical ($f = 600$ mm) and cylindrical ($f = -25$ mm, $f = 100$ mm) lenses to produce a 0.5 mm thin planar laser sheet approximately 60 mm high which passed through the flame axis of symmetry. The sheet used for LII had a fluence of approximately 0.15 J/cm^2 ± 20%, measured to be beyond the LII threshold. The LII signals from 532 nm excitation were detected perpendicular to the incident laser sheet by an intensified interline frame transfer CCD camera (Dicam Pro, PCO, 1280 × 1024 pixels) at 5 Hz and equipped with the same camera lens and filter introduced in the experimental section on LII. This LII data is only used for correlation with PIV data since the intent of the experiment was simultaneous measurements of PIV and LII using the same excitation laser.

The PIV signal was detected simultaneous to the LII signal through the use of a dichroic mirror. An interline frame transfer CCD (Imager Intense, LaVision GmbH, 1376 × 1040 pixels) was equipped with a 1 nm bandpass filter (532 FS02, Andover Corporation) transmitting the PIV radiation entered at $\lambda = 532$ nm and a Nikon camera lens ($f = 50$ mm, F8.0) fitted with a mechanical shutter (LaVision GmbH, Model 1108323) with a close time of approximately 7 ms. The interline transfer chip on this CCD allows

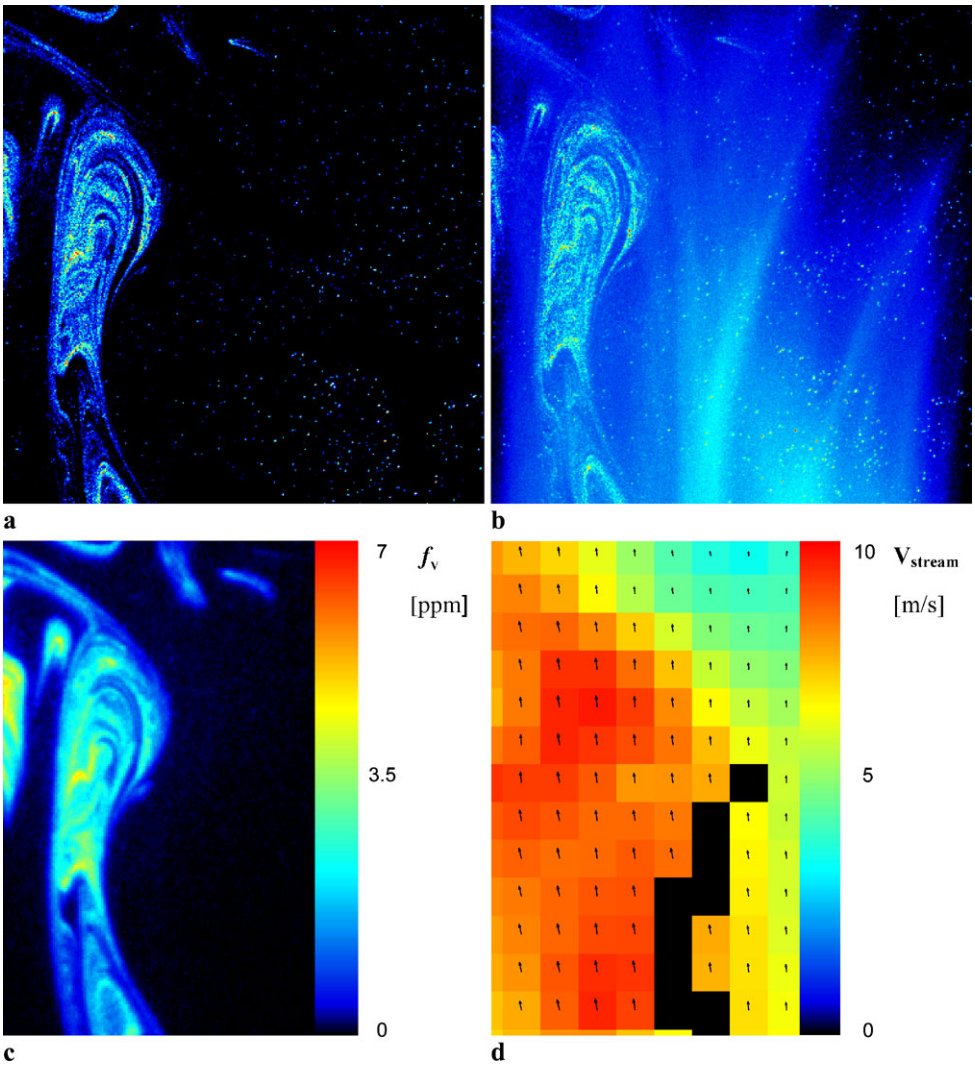

Fig. 6 Images acquired by the Imager Intense camera during PIV measurements. The first frame **a** has very little flame luminescence due to its very short effective exposure time. The second frame **b** is affected by flame luminescence, but particles are still discernible. The corresponding LII image is shown in **c**. The calculated velocity flow field is shown in **d**

for the acquisition of two frames in quick succession, the first with an exposure time as short as 3 µs, and the second with an exposure time equal to the readout time for the first image (100 to 150 ms).

Both the fuel and the co-flow streams were seeded with titanium dioxide (TiO_2) particles with a nominal diameter of 0.5 µm via a particle seeder (Particle Blaster 100, LaVision GmbH). The PIV vectors were obtained by cross-correlating the raw images using the DaVis 7 software (LaVision GmbH). The DaVis multi-pass algorithm with interrogation windows decreasing in size from 128 × 128 to 32 × 32 pixels and 50% overlap was used to process the PIV images. The resulting vector resolution was 2.4 mm, yielding a vector spacing of 1.2 mm. This resolution is insufficient to resolve the smallest turbulent length-scales in the jet, but was quite sufficient for the medium and larger spatial scales in the flame region. Additionally, it was sufficient to visualize the interaction of ambient air with the flame gases allowing better evaluation of the experiment's boundary conditions. No post-processing (e.g. smoothing, interpolating) was performed after finding the vectors beyond median filtering and 3 × 3 pixel smoothing inherent to the DaVis PIV multi-pass post-processing algorithm. Perspective distortion was measured using a dual-plane, three-dimensional imaging target (LaVision Type 7) and corrected using a third-order polynomial fit as implemented by the DaVis software calibration algorithm. The same target was used with the DaVis software calibration algorithms to map the fields of view of the PIV and LII systems to one another.

The difficulty in obtaining PIV measurements in a highly-sooting flame is due to flame luminosity, which can overwhelm the scattered laser signal from the PIV seeding material. The equipment used in this research (narrow bandpass filter and mechanical shutter) were not able to completely eliminate flame luminosity in the second (long exposure time) frame of the PIV acquisition sequence. Figure 6(a) and (b) shows example images of a highly-sooting region (the peak is ∼7 ppm) high in the flame ($h = 370$

to 400 mm). Note that the intensity scale of these images has been adjusted to make the seed particles more visible. The narrow bandwidth of the PIV camera filter and the non-intensified nature of the PIV camera indicate that the visible structures in (a) are the result of laser scattering of the PIV laser by the soot. The distinct nature of the same structures in (b), contrasted with the large blurred zone (due to flame luminosity) reinforce the conclusion that the distinct structures are due to laser-scattered soot. Figure 6(c) is the corresponding LII image. Figure 6(d) is the vector flow field, with false-color representing the streamwise velocity at each grid point. The black grid points are locations where no valid vector was found, and are notably in the region of highest flame luminosity as seen in (b).

3 Results and discussion

3.1 Images of soot and OH*

Figure 7 shows (a) processed two-dimensional images of the time-averaged chemiluminescent OH* signal, (b) an inverse Abel-transformed OH* distribution, (c) a compilation of single-shot images of soot concentration and (d) the mean soot concentration.

The OH* concentration is of minor interest for soot modeling up to this point, due to its complexity and the accompanying uncertainties concerning its role in flame reaction mechanisms [53]. OH* is, however, identified as indicator of heat release and serves as a marker for flame zones making it quite valuable for practical applications and to determine global flame characteristics. Moreover, it is important for symmetry tests prior to and during the experiment. It should be noted that the background-corrected image in Fig. 7(a) is based on the optically-integrated time averaged chemiluminescence intensity in the direction of the depth of the flame and, therefore, does not represent a 3D spatial distribution. The Abel-transformed result for the time-averaged measurement is shown in Fig. 7(b), presenting a highly-symmetric OH* distribution in the outer region along the complete flame height. Since the Abel inversion is performed from both sides to the center of the flame, axi-symmetry is verified. Note, however, that each image section for all two-dimensional measurements presented here was collected at a different time and pieced together to provide a composite representation of the flame. Taking this into account, the continuity across the individual images making up the composite image also demonstrates the temporal stability of the time averaged OH* chemiluminescence.

The results from the LII measurements performed simultaneous to the OH* measurements are shown in the latter two images Fig. 7(c) and Fig. 7(d). Images were corrected for background flame luminosity and scaled for camera gain settings. To match measured soot concentrations in the overlap regions of two sheet positions, only minor corrections (less than the typical LII uncertainty) were performed. Figure 7(c) shows a representative random collection of instantaneous soot concentration images. Figure 7(d) shows a collage of the averaged soot volume fraction measurements, f_V, for the full flame length. This collage is used for determination of axial as well as radial distributions of f_V discussed in later sections of this report. The overall shape of

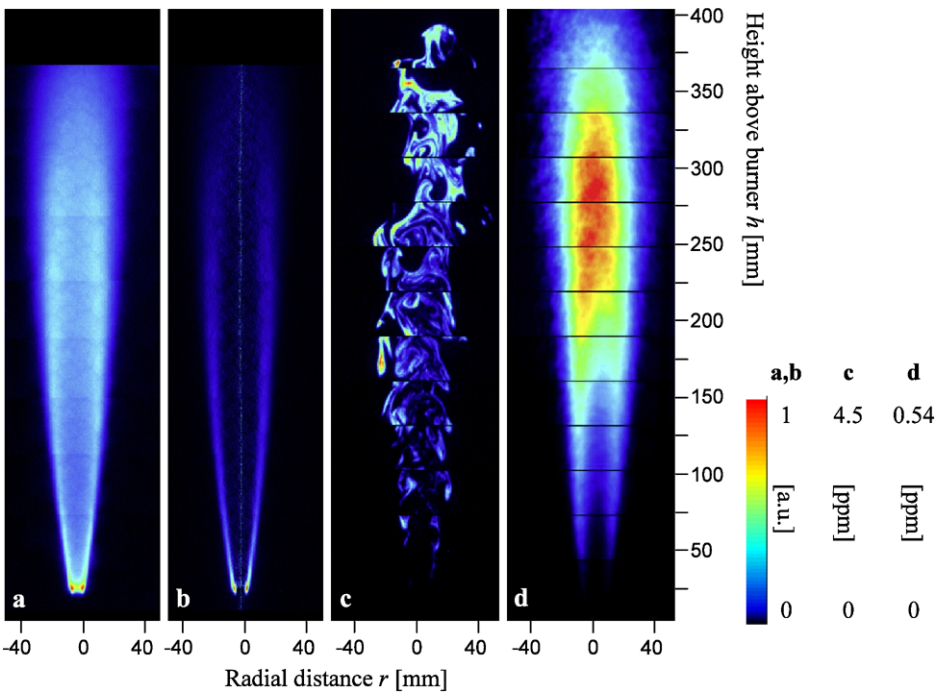

Fig. 7 False color images: **a** Averaged OH* chemiluminescence image. **b** OH* chemiluminescence image after Abel-Inversion. **c** Selective representative random selection of instantaneous LII images; the max soot concentration of 4.51 ppm is valid for this random set. Other single events were detected with higher concentration in the upper flame part. **d** Averaged 2D-LII over 1000 single images with a maximum averaged soot volume fraction of 0.54 ppm

the soot volume fractions shows a slight asymmetry with greater soot concentrations on the left (laser entry) side. The OH* chemiluminescence and the velocity field shown in later sections of this paper do not indicate any noticeable deviations. In principle, this asymmetry might be a direct result of an uneven burner nozzle construction, appearing only in the sensitive process of soot formation. However, it seems more likely that this behavior is associated with beam steering decreasing the local fluence of the laser sheet as it passes through the turbulent flame, as reported by Zerbs et al. [40]. In addition, high soot concentrations found here could lead to laser extinction along the flame path. Both effects contribute to modifications of the instantaneous local laser fluence, but can not be separated or even monitored easily. Considering the estimated errors for the soot volume fraction, the results are considered symmetric within the diagnostic limitations.

The maximum locally-averaged soot volume fraction, $f_{V,max}$, was found to be 0.54 ppm at 290 mm height above the burner (h) on the flame axis, whereas the maximum of the instantaneous images in Fig. 7(c) is 4.5 ppm. Even higher soot concentrations were detected amongst all the single-shot images. The soot distributions and soot volume fractions are in good agreement with similar jet flames investigated by Qamar et al. [33] and others as mentioned above [25, 31].

Looking at the two-dimensional image in Figs. 7(c) and 7(d), comparison of the instantaneous and averaged soot concentrations provides insightful information on the structure of the soot particle field. First, as recently discussed by Lee et al. [25], and less recently mentioned by Dasch and Heffelfinger [54], measurements of instantaneous soot volume fractions in turbulent flames show that the maximum observed soot volume fraction is one to two orders of magnitude greater than the maximum of the temporally-averaged values. For unsteady laminar flames, Hentschel et al. studied this effect in detail during forced flame oscillations [55]. It is widely accepted and evident from single-shot images that this is caused by two effects: the highly-wrinkled structure of turbulent flames and the spatial isolation of the soot structures. Secondary, as discussed by others (for example [25, 36]), soot filaments are highly intermittent and spatially isolated in the flame. The data presented here agrees with the conclusions of Lee et al. that the soot formation process in turbulent flames does not occur as a spatially continuous process, as observed in laminar flames. Soot is typically formed in turbulent flames when the temperature is between 1200 and 1800 K with the peak soot volume fractions formed between 1500 and 1600 K [28]. It also has been observed that for smaller soot volume fractions the probability density function (PDF) of the temperature tends to become progressively broader [28] resulting from a rather turbulent velocity field. Thus, the soot field structure is determined by the turbulent velocity field, which affects the spatial distribution of soot precursors and particles, and the temperature influence on the chemical formation process.

As shown here, these instantaneous single-shot images give a more comprehensive picture of the soot formation than the averaged data and are important in understanding how soot affects combustion devices.

3.2 Soot volume fraction profiles

The axial profile of the averaged soot volume fraction from 1064 nm excitation is shown in Fig. 8(a). It is clear that the concentration of soot within the sheets increases from the bottom of the flame and is passing a maximum of 0.54 ppm near $h = 300$ mm. After the maximum, the average f_V decreases faster than it rose. Investigations by Lee et al. [25] produced results similar to the profiles shown here.

Comparing the averaged behavior with single-shot events for soot concentration shown in Fig. 7, the instantaneous soot volume fraction increases similarly to the averaged values with increasing height, but remains relatively high through the burnout region at the tip of the flame. Soot events are rarer at the flame tip compared to the lower parts of the flame. However, when the wrinkled soot structures

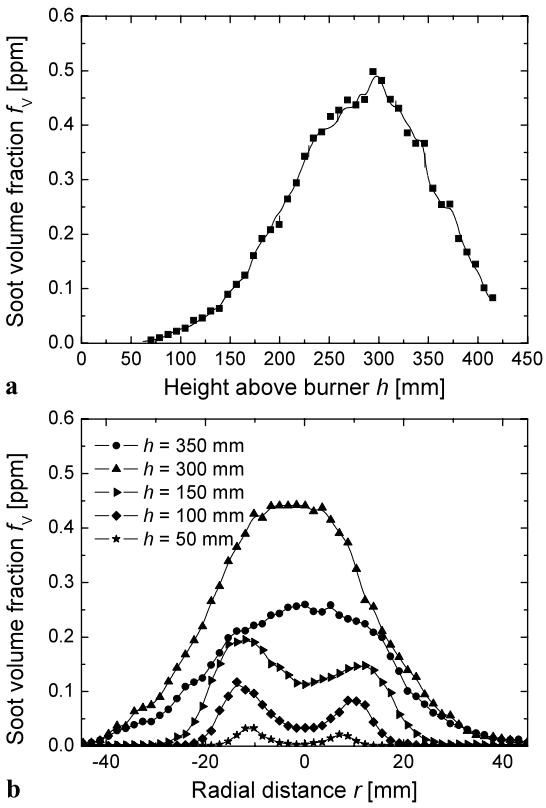

Fig. 8 **a** Axial profile of the average soot volume fractions f_V on the jet axis. **b** Radial profiles of the average soot volume fractions f_V for different heights above burner. The curves in the figure are cubic spline fits to the data

exist in these locations, they are much larger than elsewhere and exhibit higher soot concentrations. The decrease in the mean soot volume fraction in the flame tip region implies that the occurrence of these events decreases faster than the instantaneous soot volume fraction increases [36].

Radial profiles of the average soot volume fraction are shown at discrete heights of $h = 50$, 100, 150, 300, and 350 mm in Fig. 8(b). The radial profiles show two peaks for heights below 150 mm. Further downstream these peaks merge into a single peak along the jet axis, consistent with the results of [25] and [28]. The single events do not show this behavior on first inspection. In the lower part of the flame, smaller wrinkled structures close to the jet burner axis are apparent, while with increasing height the structures are more dispersed in the horizontal direction. A statistical analysis similar to [36] may provide more details, but is unfortunately beyond the scope of the current work.

3.3 Temperature data

A comprehensive data set of single-shot flame temperature was obtained by SV-CARS measurements. The spectra had good signal-to-noise ratios throughout the flame resulting in temperature measurements with high precision. The only exception was in the flame tip region, which will be discussed in a subsequent section.

The temperature measurement locations are made up of 33 locations along the burner axis (with special focus on the initial soot formation zone) and four radial profiles at heights of $h = 63$, 113, 213, and 413 mm above the burner. Each measurement location consisted of 1200 single-shot CARS measurements resulting in a PDF of 1200 temperature values.

Example PDFs are shown in Fig. 9 for two characteristic flame regions on-axis at $h = 44$ mm and at $h = 250$ mm. The mean temperatures (T_{mean}) and most probable temperatures (T_{mopro}) were determined from these PDFs. Whereas T_{mean} considers all the evaluated temperature information without any weighting, the most probable temperature T_{mopro} and the 90% interval of all temperatures are more suitable to represent the temperature fluctuations [56]. Note that the error bars indicate the range containing 90% of all single-shot temperature values and are thus indicative of the width of the temperature PDF. Good signal-to-noise ratios in the CARS spectra allow for evaluation of almost each single measurement with high accuracy. The number N of evaluated spectra is smaller than the number of recorded spectra 1200 because some spectra were rejected due to a too low intensity (bad signal-to-noise ratio), a too high intensity (saturation of the A/D converter), or a too large sum of residuals (bad quality of the spectrum) [56]. Figures 9(a) and 9(b) show typical results, where out of 1200 single events 1128 and respectively 1193, were fitted.

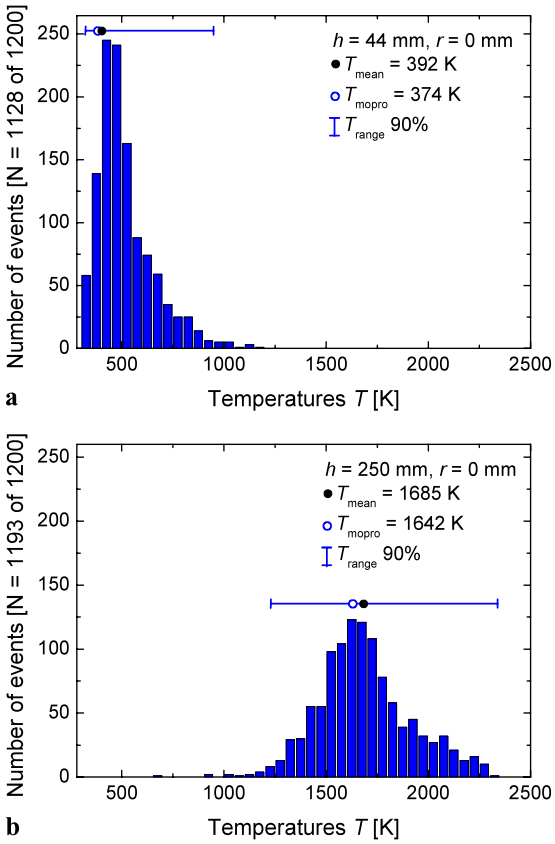

Fig. 9 Probability Density Function for mean and most probable (mopro) temperature as well as the range covering the most probable 90% of all instantaneous temperatures. Total number of analyzed laser pulses is 1128 and 1193 out of 1200, respectively; the examples show typical measurement locations at **a** heights of 44 mm and **b** 250 mm on burner axis

Comparison of the two PDFs in Fig. 9 shows a change of both the 90% temperature range and the shape of the temperature distribution. The distribution in Fig. 9(a) for $h = 44$ mm consists of a steep low temperature wing with a significantly flatter high temperature wing. With increasing height in the flame, the maximum is shifted to higher values, while the distribution becomes wider and less localized. This corresponds with the increase in flow turbulence, generating fluctuations typical for non-premixed turbulent jet flames and is similar to the effects seen in the single-shot LII images. To detect these trends more clearly, T_{mean} and T_{mopro} are plotted for each location on the flame axis with the temperature range as error bars in Fig. 10.

In Fig. 10(a) the mean temperatures on the burner axis rise to a maximum of 1728 K at a height of $h = 300$ mm above the burner. Up to this point, there is a fairly good agreement between T_{mean} and T_{mopro}. For the lower flame region, temperature fluctuations of 100 K are typical, increasing steadily with height. High fluctuations in the flame tip region at $h = 400$ mm cover a wide range of temperatures from 956 to 2077 K. Combining this with the strong

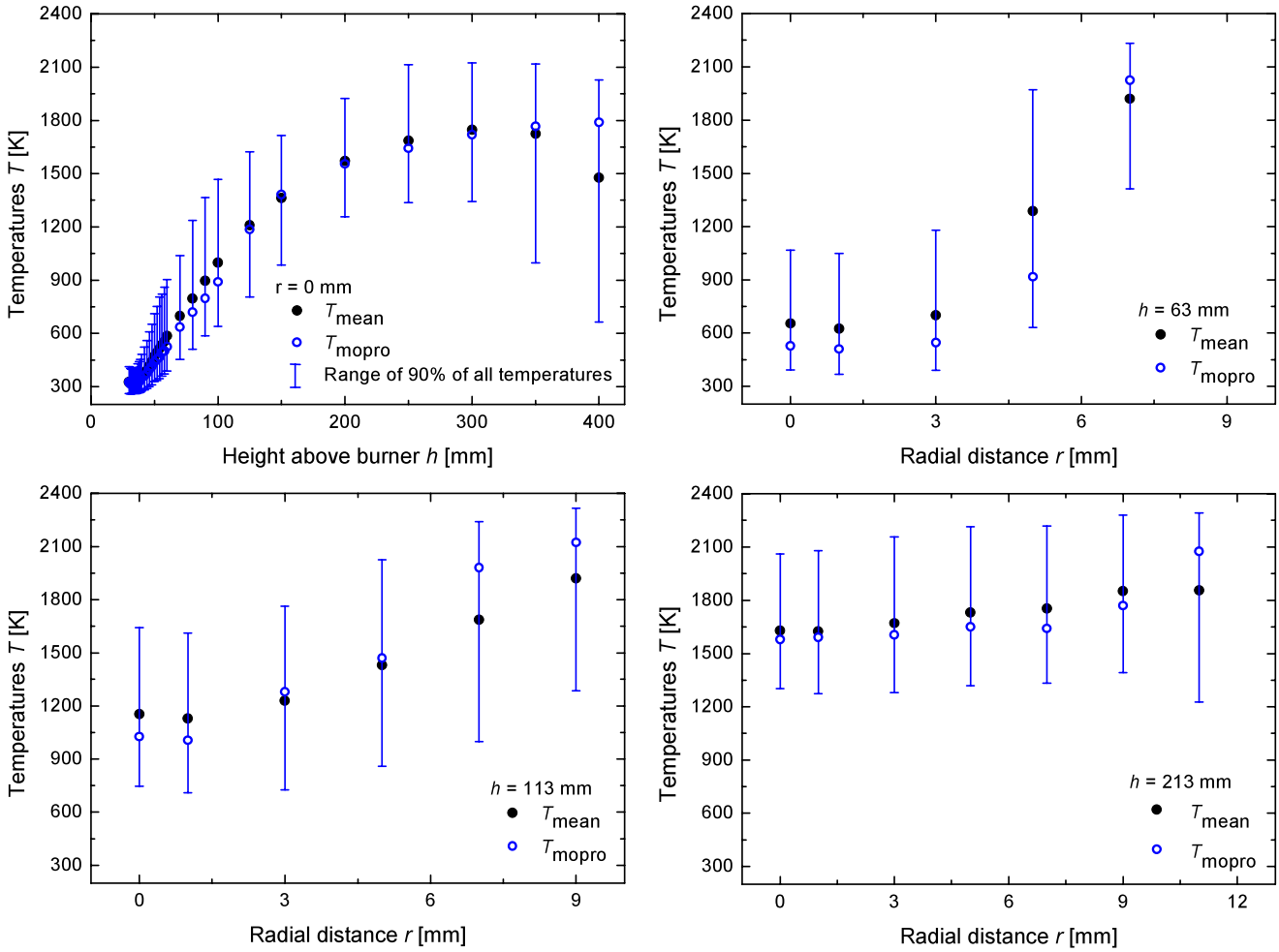

Fig. 10 CARS temperature profiles. **a** Axial profile; **b** Radial profile $h = 63$ mm; **c** Radial profile $h = 113$ mm; **d** Radial profile $h = 213$ mm. Mean (T_{mean}) and most probable (T_{mopro}) temperatures are shown. *Blue bars* indicate the temperature interval containing 90% of all events. PDFs are available for all measurement locations

fluctuations shown in the single-shot LII-images leads to the conclusion that there is strong turbulence intensity in this region.

A large dynamic range for the temperature measurements has an unexpected influence on the mean temperature. Above a height of $h = 300$ mm, the mean temperature decreases significantly. This occurs as a result of being forced to decrease the CCD gain to capture cold spectra at the cost of losing low signal levels for high-temperature regions in the highly dynamic flame tip part. Careful analysis indicates that the higher values for the mean temperatures were probably under predicted, resulting in a systematic lower mean value in the flame tip region. Roughly half of the 1200 measurements in this region were rejected due to low signal intensity attributed to the high temperatures. Calculation of T_{mopro} however, gives a more realistic behavior resulting in a slight increase of the most probable temperature even in the upper flame regions and is recommended for model validation purposes. The bias resulting from exclusion of low intensity spectra from the analysis is qualitatively accessible through the analysis' statistics.

Three radial profiles for $r = 63$, 113 and 213 mm are plotted in Fig. 10(b)–(d). The first two profiles at $h = 63$ mm and 113 mm show an increase of the mean temperature with increasing radial distance. This effect is more pronounced for the lower flame region (b) where the temperature increases from 600 K at flame center up to 2000 K at the periphery. With increasing height, the mean centerline temperature for $r = 213$ mm rises significantly, decreasing the radial temperature range since only a slight increase in temperature is observed at the outer periphery. The radial temperature profile for $h = 413$ mm, not shown here, reveals increasing temperature fluctuations further away from the flame centerline. The observed temperature range at a single point in space reaches the limitation of the current CARS setup resulting in biased quantitative data for this region making the upper flame tip region not de-

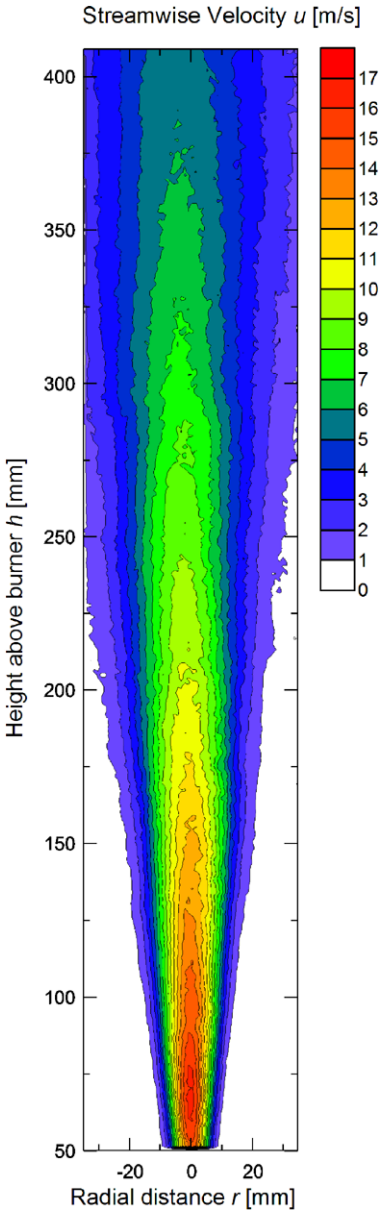

Fig. 11 Time-averaged streamwise velocity contours for the visible flame region

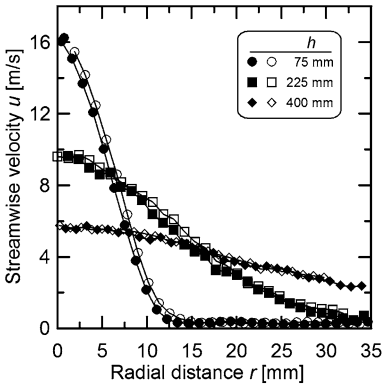

Fig. 12 Profiles of streamwise velocity plotted versus the absolute value of the radial distance from the burner center at three heights above burner. *Hollow symbols* indicate the left side of the axis of symmetry from Fig. 11, *solid symbols* indicate the right side

sirable for validation purposes. The measurements indicate large fluctuations raging from 400 to 2000 K for the flame tip.

Measurements made for the sole purpose of symmetry validation and data cross checking are not shown. The measured temperature field includes at least one location in the opposite half of the flame for every radial profile taken. The mean temperatures for the $r = +7$ mm and -7 mm position at $h = 63$ mm differ by 31 K. The largest differences were found to be 90 K for the highly dynamic region of $r = \pm 5$ mm at $h = 213$ mm. Overall, agreement across the axis of symmetry was good.

3.4 Planar flow field measurements

Two hundred PIV measurements were made centered at eight different heights above the burner and stitched together to produce Fig. 11, which shows the time-averaged streamwise velocity for the visible flame region. The jet velocity is symmetric about the centerline, as can be seen in Fig. 12, where streamwise velocity profiles beginning from $r = 0$ mm at three heights above the burner are shown.

For a single imaging height (from $h = 100$ to 130 mm), 2000 higher magnification PIV measurements were made to calculate the ensemble-averaged turbulence intensities in the streamwise (u'rms/$\bar{u}$) and radial (v'rms/$\bar{u}$) directions. After removal of spurious vectors, 1268 vectors remained at each of 20 heights above the burner for a total of more than 25 000 measurements. The streamwise turbulence intensity was found to fall between a maximum of 22% (with no additional filtering) and a minimum of 15% (after filtering the ensemble to a range of plus or minus three times the standard deviation of the set) within the tested range of heights above the burner. The same process performed, using the radial turbulence intensity, yielded a maximum of 14% (with no additional filtering) and a minimum of 10.5% (after $\pm 3\sigma$ filtering).

3.5 Simultaneous PIV/LII experiment

Parallel to the PIV experiments, simultaneous LII detection was performed using 532 nm as excitation wavelength. Excitation at this wavelength presents challenges for quantified soot measurements, since PAH interferences are known to be present in the visible range [40]; however, the usage of 532 nm is necessary for the simultaneous PIV measurements. While a preliminary comparison of the two LII data sets for selected radial profiles showed only minor deviations, it is recommended that 1064 nm excitation LII data

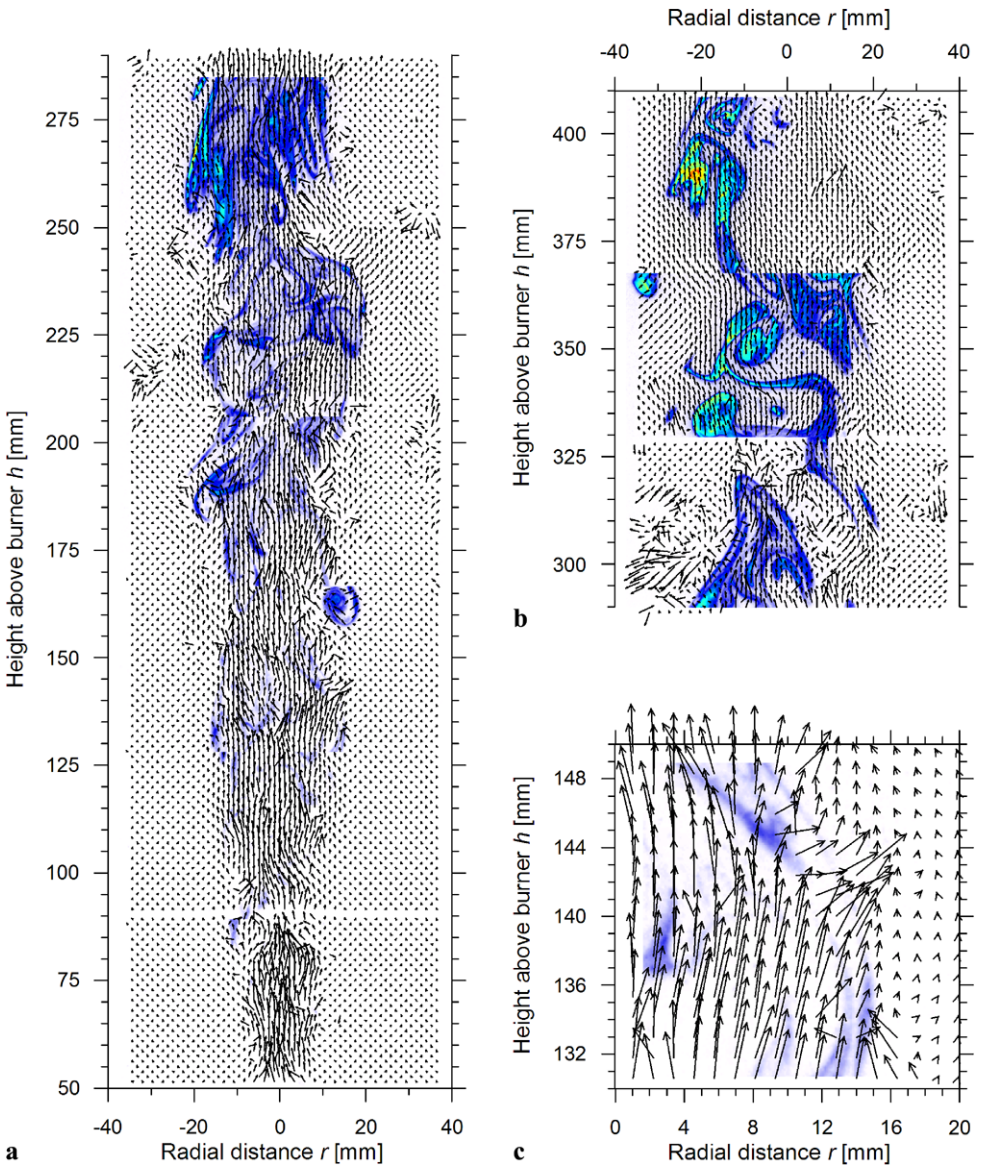

Fig. 13 Simultaneous PIV and LII data on a shot-to-shot basis in heavily sooting turbulent flame. The false color scheme instantaneous soot structures are overlaid with simultaneous vector field for the same region. **a** Shows the bottom part of the flame, while **b** shows the top part. **c** Image shows an expanded zone from **a** with a strong fluid velocity across a high-sooting region

presented above be used for model validation purposes. Figures 13(a) and 13(b) show a collage of simultaneous PIV and LII measurements stitched together to form a single image containing instantaneous information on soot concentration and velocity field. The figure is divided into the bottom portion of the flame (a) and the top portion of the flame (b) due to its large aspect ratio. Also, every second vector in both the streamwise and radial direction has been removed for clarity.

Figure 13(c) shows a small region of Fig. 13(a) to give the reader a better sense of the available spatial resolution and the quality of the data at hand. The region in Fig. 13(c) was also chosen as an example of a zone with a strong fluid velocity across a high-sooting region, perhaps indicating a break in the flame front. This was seen only intermittently, but unfortunately, a complete statistical analysis of this data is beyond the scope of this paper.

4 Summary and conclusions

The current presentation of data is intended to provide a comprehensive characterization of a highly sooting, turbulent jet flame specifically designed to permit the evaluation of soot models. Reproducibility, simplicity, high soot concentrations, and exact definition of boundary conditions were emphasized, leading to the simple, non-premixed ethylene jet flame.

Detailed and accurate measurements of quantitative soot properties and the temperature field were obtained on an average and instantaneous basis to provide a high quality

dataset including the measured parameters and their statistics. Additional, i.e. not shown PDF temperature data were obtained, but have not been included due to space restrictions, but is available upon request. Complementing these measurements, a series of PIV measurements were performed to characterize the average velocity field characteristics.

While soot maps and statistics for the newly-defined turbulent flame reproduce features known from literature, the value of the current activities is the combination of these data with detailed temperature and flow field maps providing an exhaustive basis for model validation purposes. Similar to literature, evaluation of the average and instantaneous soot concentration data showed different features in terms of magnitude and distribution, leading to the conclusion that the instantaneous single-shot images give a more comprehensive picture of soot formation than the averaged data and are likely necessary to fully understand how soot affects combustion devices.

Additionally, diagnostic challenges and limitations of measurements in a turbulent sooting environment are addressed and notable improvements presented. Among other technical developments and a special focus on instantaneous information, we report the first investigation of simultaneous instantaneous soot concentration and velocity field measurements in a heavily sooting environment, thereby adding to existing complementary measurement techniques in turbulent combustion. This achievement potentially provides a means to answer the question of how much the temporal/spatial statistics of soot distributions are due to flow field fluctuations rather than chemistry. High spatial and temporal dynamics of soot events throughout the flame indicate that the instantaneous interaction between the flame and the flow field is important. This leads to the conclusion that CFD modeling should not be restricted to time-averaged simulations. A more detailed analysis of the simultaneous PIV/LII measurements is beyond the scope of this paper. However, this data shall provide a better understanding of the interaction between turbulent flow and chemical soot processes.

Satisfying modelers' needs, good flame reproducibility, and simple burner geometry, in combination with a comprehensive and accurate data set, make a convincing case for suggesting this jet flame as a new standard for the investigation of turbulent sooting flames.

Acknowledgements This research was supported by the Helmholtz/NRC collaborative partnership "Fuelling a cleaner future: Quantification and characterization of soot emissions from combustion based energy conversion". The authors wish to thank Massimiliano Di Domenico, Thomas Blacha, and Peter Gerlinger for fruitful and insightful discussions. Tobias Rapp and Jens Kreeb are gratefully acknowledged for expert technical and mechanical support.

References

1. Committee on Aviation Environmental Protection, Working Group 3, CAEP/7-IP/6, Montreal, Canada (2007)
2. A. Petzold, R. Marsh, M. Johnson, M. Miller, Y. Sevcenco, D. Delhaye, X. Vancassel, A. Ibrahim, A. Veira, P. Williams, H. Bauer, A. Crayford, S. Morris, P. Kay, P. Bowen, W.D. Bachalo, D. Raper, Final report, EASA.2008.OP.13, EASA Cologne (2009)
3. Society of Automotive Engineers Inc, AIR 5892 (2004)
4. Society of Automotive Engineers Inc, AIR 6037 (2009)
5. W. Lazik, T. Doerr, S. Bake, R. von der Bank, L. Rackwitz, in *Proc. ASME Turbo Expo 2008, Power for Land, Sea and Air*, 09–13.06.2008, Berlin, Paper GT2008-51115 (2008)
6. H. Richter, M. Braun-Unkhoff, S. Granata, J. Yu, E. Goos, N. Slavinskaya, P. Frank, W. Green, J. Howard, in *Proc. European Combustion Meeting ECM2005*, Louvain-la-Neuve, Belgium, Paper 163 (2005)
7. M. Kamphus, M. Braun-Unkhoff, K. Kohse-Höinghaus, Combust. Flame **152**, 28 (2008)
8. J. Appel, M. Frenklach, H. Bockhorn, Combust. Flame **121**, 122 (2000)
9. M. Frenklach, Phys. Chem. Chem. Phys. **4**, 2028 (2002)
10. S. Granata, F. Cambianica, S. Zinesi, T. Faravelli, E. Ranzi, in *Proc. European Combustion Meeting ECM2005 (Louvain-la-Neuve, Belgium)*, Paper 035 (2005)
11. D.O. Lignell, J.H. Chen, P.J. Smith, T. Lu, C.K. Law, Combust. Flame **151**, 2 (2007)
12. I. Kennedy, W. Kollmann, AIAA J. **29**, 1452 (1991)
13. B. Zamuner, F. Dupoirieux, Combust. Sci. Technol. **158**, 407 (2000)
14. M. Di Domenico, P. Gerlinger, M. Aigner, Combust. Flame **157**, 246 (2010)
15. M. Di Domenico, PhD thesis Universität Stuttgart (2008) http://elib.uni-stuttgart.de/opus/volltexte/2008/3624/pdf/DiDomenico_Doktorarbeit.pdf
16. R.S. Barlow, Proc. Combust. Inst. **31**, 49 (2007)
17. E.P. Hassel, S. Linow, Meas. Sci. Technol. **11**, R37 (2000)
18. W.L. Oberkampf, T.G. Trucano, Prog. Aerosp. Sci. **38**, 209 (2002)
19. J.C. Oefelein, R.W. Schefer, R.S. Barlow, AIAA J. **44**, 418 (2006)
20. W. Strahle, Prog. Energy Combust. Sci. **12**, 253 (1986)
21. F.C. Gouldin, R.W. Schefer, S.C. Johnson, W. Kollmann, Prog. Energy Combust. Sci. **12**, 257 (1986)
22. G.M. Faeth, S.G. Samuelsen, Prog. Energy Combust. Sci. **12**, 305 (1986)
23. M.C. Drake, W. Kollmann, Prog. Energy Combust. Sci. **12**, 373 (1986)
24. TNF Workshop web site, available at http://www.ca.sandia.gov/TNF Sandia National Laboratories (2010)
25. S.-Y. Lee, S.R. Turns, R.J. Santoro, Combust. Flame **156**, 2264 (2009)
26. J.H. Kent, S.J. Bastin, Combust. Flame **56**, 29 (1984)
27. J.H. Kent, D. Honnery, Combust. Sci. Technol. **54**, 383 (1987)
28. A. Coppalle, D. Joyeux, Combust. Flame **96**, 275 (1994)
29. R.P. Lindstedt, S.A. Louloudi, Proc. Combust. Inst. **30**, 775 (2005)
30. R.L. Vander Wal, Exp. Fluids **23**, 281 (1997)
31. S.J. Brookes, J.B. Moss, Combust. Flame **116**, 49 (1999)
32. A. Kronenburg, R.W. Bilger, J.H. Kent, Combust. Flame **121**, 24 (2000)
33. N.H. Qamar, G.J. Nathan, Z.T. Alwahabi, K.D. King, Proc. Combust. Inst. **30**, 1493 (2005)
34. Y. Xin, J.P. Gore, Proc. Combust. Inst. **30**, 719 (2005)
35. C.R. Shaddix, J. Zhang, R.W. Schefer, Conference Paper LACSEA, OSA (2010)
36. N.H. Qamar, Z.T. Alwahabi, Q.N. Chan, G.J. Nathan, D. Roekaerts, K.D. King, Combust. Flame **156**, 1339 (2009)

37. R. Hadef, K.P. Geigle, W. Meier, M. Aigner, Int. J. Therm. Sci. **49**, 1457 (2010)
38. C.K. Westbrook, F.L. Dryer, K.P. Schug, Proc. Combust. Inst. **19**, 153 (1998)
39. R.J. Santoro, C.R. Shaddix, in *Applied Combustion Diagnostics*, ed. by K. Kohse-Höinghaus, J.B. Jeffries (Taylor & Francis, New York, 2002)
40. J. Zerbs, K.P. Geigle, O. Lammel, J. Hader, R. Stirn, R. Hadef, W. Meier, Appl. Phys. B **96**, 683 (2009)
41. T.T. Charalampopoulos, J.D. Felske, Combust. Flame **68**, 283 (1987)
42. R.A. Dobbins, G.W. Mulholland, N.P. Bryner, Atmos. Environ. **28**, 889 (1994)
43. K.C. Smyth, C.R. Shaddix, Combust. Flame **107**, 314 (1996)
44. M. Schnaiter, H. Horvath, O. Möhler, K.-H. Naumann, H. Saatho, O.W. Schöck, J. Aerosol Sci. **34**, 1421 (2003)
45. D.R. Snelling, F. Liu, G.J. Smallwood, Ö.L. Gülder, Combust. Flame **136**, 180 (2004)
46. D.R. Snelling, G.J. Smallwood, F. Liu, Ö.L. Gülder, W.D. Bachalo, Appl. Opt. **44**, 6773 (2005)
47. A. Coderre, Master thesis, Carlton University, Ottawa (2009)
48. C.J. Dasch, Appl. Opt. **31**, 1146 (1992)
49. K.P. Geigle, Y. Schneider-Kühnle, M.S. Tsurikov, R. Hadef, R. Lückerath, V. Krüger, W. Stricker, M. Aigner, Proc. Combust. Inst. **30**, 1645 (2005)
50. B.M. Crosland, M.R. Johnson, K.A. Thomson, Appl. Phys. B (2010) doi:10.1007/s00340-010-4130-7
51. R. Puri, T.F. Richardson, R.J. Santoro, R.A. Dobbins, Combust. Flame **92**, 320 (1993)
52. M.S. Tsurikov, K.P. Geigle, V. Krüger, Y. Schneider-Kühnle, W. Stricker, R. Lückerath, R. Hadef, M. Aigner, Combust. Sci. Technol. **177**, 1835 (2005)
53. T. Kathrotia, M. Fikri, M. Bozkurt, M. Hartmann, U. Riedel, C. Schulz, Combust. Flame **157**, 1261 (2010)
54. C.J. Dasch, D.M. Heffelfinger, Combust. Flame **85**, 389 (1991)
55. J. Hentschel, R. Suntz, H. Bockhorn, Appl. Opt. **44**, 6673 (2005)
56. O. Lammel, H. Schütz, G. Schmitz, R. Lückerath, M. Stöhr, B. Noll, M. Aigner, M. Hase, W. Krebs, J. Eng. Gas Turbine Power **132**, 121503 (2010)